Deep Depth from Aberration Map

Masako Kashiwagi[1] Nao Mishima[1] Tatsuo Kozakaya[1] Shinsaku Hiura[2]
[1]Toshiba Corporate Research & Development Center [2]University of Hyogo
{firstname.lastname}@toshiba.co.jp hiura@eng.u-hyogo.ac.jp

Abstract

Passive and convenient depth estimation from single-shot image is still an open problem. Existing depth from defocus methods require multiple input images or special hardware customization. Recent deep monocular depth estimation is also limited to an image with sufficient contextual information. In this work, we propose a novel method which realizes a single-shot deep depth measurement based on physical depth cue using only an off-the-shelf camera and lens. When a defocused image is taken by a camera, it contains various types of aberrations corresponding to distances from the image sensor and positions in the image plane. We call these minute and complexly compound aberrations as Aberration Map (A-Map) and we found that A-Map can be utilized as reliable physical depth cue. Additionally, our deep network named A-Map Analysis Network (AMA-Net) is also proposed, which can effectively learn and estimate depth via A-Map. To evaluate the validity and robustness of our approach, we have conducted extensive experiments using both real outdoor scenes and simulated images. The qualitative result shows the accuracy and availability of the method in comparison with a state-of-the-art deep context-based method.

1. Introduction

Single-shot depth measurement using an off-the-shelf camera is still an open problem despite remarkable advances in computational photography. In particular, the simultaneous pursuit of high robustness, low cost, and high depth accuracy are challenging requirement for realizing production.

For the single-shot approach, deep monocular depth estimation (DMDE) [17, 2] and depth from defocus (DfD) [5, 14, 7, 19, 23, 25, 24] are mainly proposed in recent years. DMDE is the most successful method, has greatly advanced the accuracy of depth estimation by extracting contextual information with a deep learning technique. Despite the re-

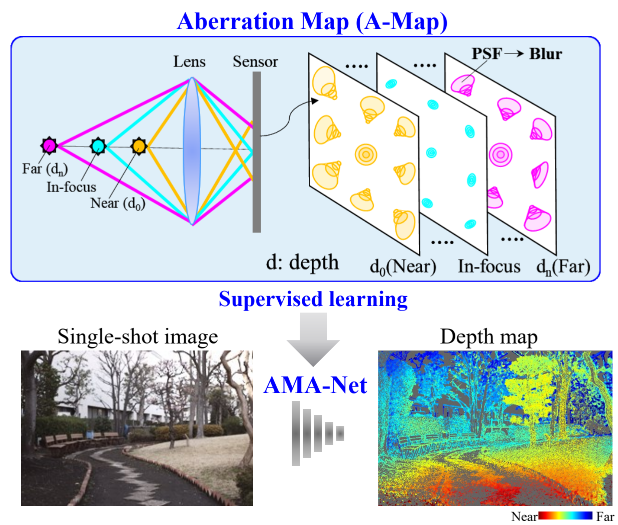

Figure 1. Depth measurement from a single-shot image by supervised learning of Aberration Map (A-Map) which contains various types of aberrations, position of image, and distance information.

markable progress of DMDE, it has a fundamental limitation that a correct depth map cannot be estimated without sufficient contextual information, for instance, in a scene without the ground because it does not incorporate physical depth cues. Conversely, single-shot DfD estimates depth by purely simulating a model of defocus blur, without utilizing contextual information. Although the depth cue is physically given as defocus blur, the depth still has the near side or far side ambiguity from the focal plane. While several proposals which insert different types of color filters [5, 7, 23, 25, 24] into the lens aperture solve this problem. Another approach of single-shot DfD focuses on axial chromatic aberration [28, 9]. However, these approaches need hardware customization to generate the desired aberration. Moreover, it is difficult to model the actual point spread functions (PSFs) because a camera lens generally contains various types of aberration. Recently, a combination of DMDE and DfD named as deep depth from defocus (DDfD) is proposed in [22]. Its main idea is to improve depth estimation by deep learning both defocus blur based on DFD and contextual information. DDfD shows that out-of-focus blur helps to improve the depth accuracy but it still depends on contextual information and thus unavoidable the inherent limitation of DMDE.

Since the actual aberrations are very minute and complex in comparison with contextual information and defocus blur, there has not been investigated yet how they affect depth measurement, regarding to such both on-axis aberrations and off-axis aberrations. Through our PSF measurement experiment, we observed that actual defocused PSF shapes produced by an off-the-shelf camera lens are unique with respect to the distance from the image sensor and it also has a position dependence in the image plane. We call an image which contains this position-dependent and distance-dependent aberrations as A-Map.

In this paper, we present a single-shot depth measurement method using only an off-the-shelf camera. We also propose A-Map Analysis Network (AMA-Net) which learns the relationship between A-Map and corresponding depth in a supervised manner. We demonstrate that our method outperforms a conventional method in qualitative evaluation, including various outdoor scenes. The main contributions of this paper are listed below:

- We present a novel approach of physics-based single-shot depth estimation by utilizing A-Map of an off-the-shelf lens.
- We propose an original deep network, AMA-Net, which consists of two branches, such as gradient brunch and positional brunch, and efficiently estimates depth from A-Map without involving contextual information.
- We demonstrated not only the robustness of our method through qualitative and quantitative evaluations with various outdoor textures, but also the validity of aberrations as depth cues by simulation studies.

2. Related work

One of the major methods for physics-based depth estimation is depth from defocus (DfD). DfD is a passive depth estimation based on modeling a defocus blur radius. A blur radius b is derived from the lens-maker's formula,

$$b = \frac{av_f}{2p}\left|\frac{1}{f} - \frac{1}{u} - \frac{1}{v_f}\right|, \quad (1)$$

where u, $a = \frac{f}{F}$, f, F, p and v_f are an object's distance, a diameter of the lens aperture, a focal length, an aperture number, a sensor pitch and a distance between the lens and the image sensor, respectively. Although the depth cue is physically given as defocus blur, the depth still has the ambiguity of near side or far side of the focal plane, because there is same blur radius in both planes. Thus, DfD method usually uses more than two-shot images to estimate the blur radius [27].

For single-shot depth estimation with physical depth cue, there are several proposals of color-coded apertures (CCA) which insert different types of color filters [5, 14, 7, 19, 23, 25, 24] into a lens aperture. Another approach for generating depth cue in [28] is focusing on axial chromatic aberration (ACA) by using customized chromatic lens. Although CCA and ACA can solve the depth ambiguity, they require hardware customization to obtain sufficient physical depth cue.

In recent years, deep learning approaches have greatly advanced in computer vision, and there is no exception for depth estimation. One of the successful methods is DMDE [17, 2]. Generally, deep neural network is trained with a large RGB-D dataset to learn variation of contextual information. However, this method has limitation of using images in the wild, for instance, in a scene without the ground, sky or simple pattern such as a stripe.

The method of [22] combines DMDE with DfD to improve depth estimation. They investigate that defocus blur can be utilized as an additional depth cue. Although they present great potential of blur information as physical depth cues besides contextual information, it still depends on contextual information and is not yet detailed enough to analyze blur information.

3. Method

The key point for accurate depth estimation is to find the physical depth cues which should be unique within measured distances. To investigate various types of aberrations can be utilized as a depth cue, first we describe lens aberration in Section 3.1 and then explain A-Map with measuring and analyzing PSFs of an RGB camera lens in Section 3.2. Finally, our deep network, A-Map analysis network (AMA-Net) is proposed in Section 3.3.

3.1. Lens aberrations

Lens aberrations are generally categorized as chromatic aberrations (CA) and monochromatic aberrations (MA). As CA, there are two types such as axial chromatic aberrations (ACA) and transverse chromatic aberrations (TCA). MA is widely known as five Seidel aberrations: spherical aberrations, coma, astigmatism, curvature of field and distortion. In most cases, ACA and spherical aberrations occur at the center of the image. On the other hand, TCA and coma occur around the corner of the image. These types of aberrations depend on the angle of incidence (on or off axis) of the light on the lens.

Some types of aberrations are illustrated in Figure 2. In the case of single lens, each color, blue, green and red light has different focal length due to dispersion (Figure 2 (a)). When an object is in the far or near plane, blue or red

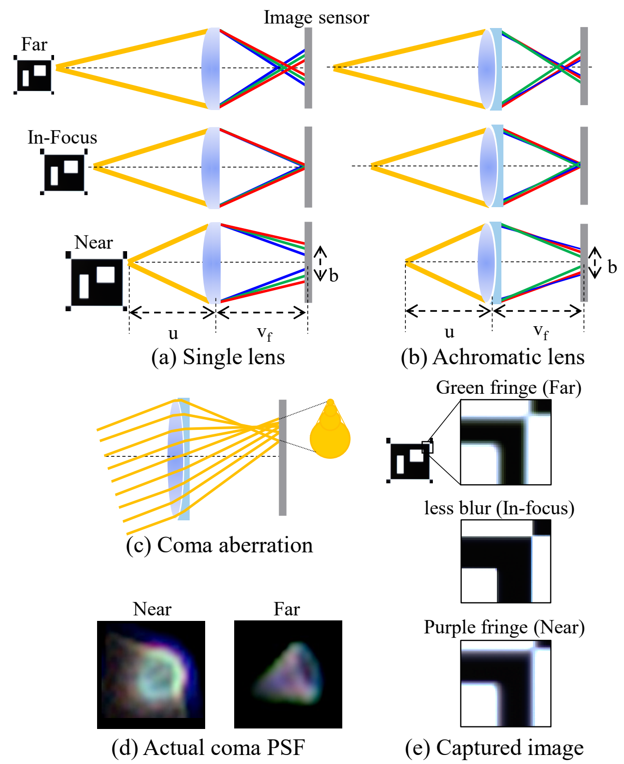

Figure 2. Various aberrations of actual lens. (a) ACA of single lens, (b) ACA of achromatic lens, (c) Coma aberration, (d) Example of actual coma PSF, and (e) Example of fringes produced by actual camera lens aberrations.

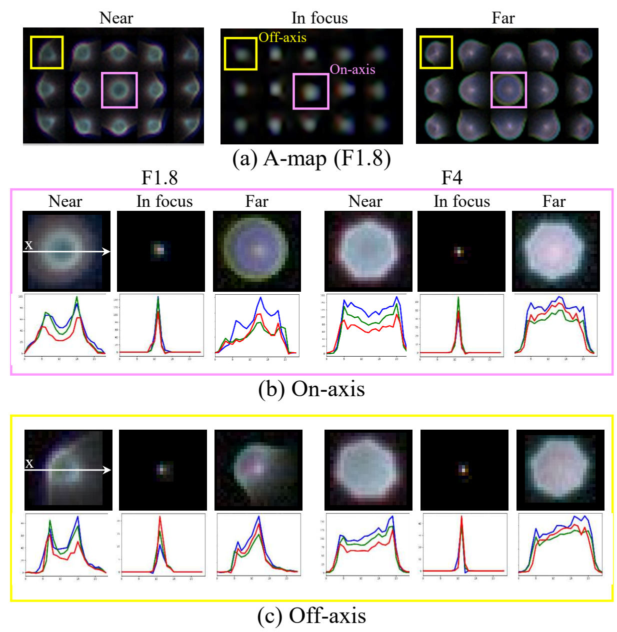

Figure 3. PSF measurement results. The point light sources were measured with f=50mm RGB-SDLR camera, F1.8 and F4, at, near, in-focus, and far side, respectively. (a) is the example of sampled A-Map F1.8. Pink and yellow square show on-axis and off-axis PSF. (b) and (c) show expanded images of the on-axis and off-axis where the position is squared in (a). The numerical values of the PSF in the horizontal direction (white arrow) are shown below the expanded PSF images.

fringe can be seen around the edge of captured images. Figure 2 (b) shows the simplest structure of achromatic lens which typically corrects red and blue light. Nevertheless, still purple and green fringes are observed in the near and far plane since CA cannot be perfectly removed. Coma aberrations are also difficult to remove and off-axis lights appear as a comet-like tail on the image plane (Figure 2 (c) and (d)). Even though a digital single-lens reflex camera (DSLR) lens has a more complex structure with many lenses, the colored-edge fringe is still visible (Figure 2 (e)).

3.2. Aberration Map

When considering the case of using product lens, blur is produced from not only ACA but also other aberrations which are hard to be suppressed perfectly. To investigate the behavior of both on-axis and off-axis aberrations at the same time, we first measure PSFs because various types of aberrations are eventually expressed in the form of PSFs. PSFs can be efficiently measured by using DSLR camera and capturing an image of point light sources (a matrix of white dots) which is displayed on high resolution display, at various distances (details are described in Section 4.1). Figure 3 shows an example of measurement results, the measurement distance was 1000mm (near), 1500mm (in-focus) and 2000mm (far). As the figure shows, PSF has a position dependence of the image.

We named these images which show the distance and position dependency of PSFs as A-Map.

Figure 3 (b) and (c) shows the results of on-axis and off-axis with F1.8 and F4. In addition, the numerical values of the PSF across horizontal direction are also shown. There are two major differences between the near-plane and the far-plane. The first one is the shape of the PSF, the overall rough shape is induced by defocusing, and the detailed shape is induced by various aberrations. For example, the near plane PSF forms a concave surface of the center portion and the far plane forms a convex surface. The second is the color fringe, the purple and green fringe is generated by CA, observed at near and far, respectively. Furthermore, the off-axis PSF's shape (Figure 3) is different from on-axis PSF, which is caused by off-axis aberrations such as TCA, coma, and field curvature.

From the measurement results, it can be observed that the shape of the PSFs of the defocused plane has corresponding distance. In addition, it is clear that the PSF of the product's camera lens is too complicated to simulate, as the PSF is generated from various kinds of aberrations. Therefore, the

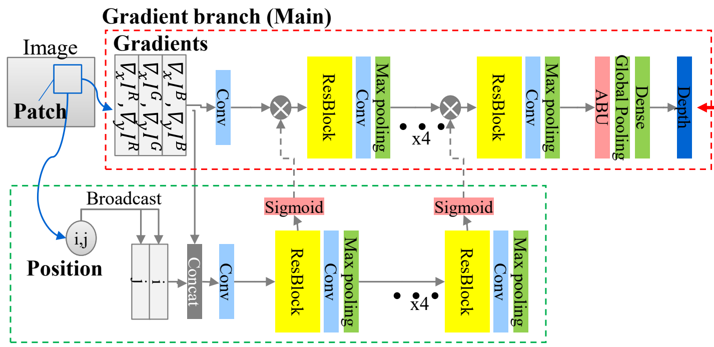

Figure 4. The architecture of AMA-Net based on ResNet. A main branch extracts blur from the gradients. A positional branch makes attention maps. The main branch feature map is multiplied by the attention maps.

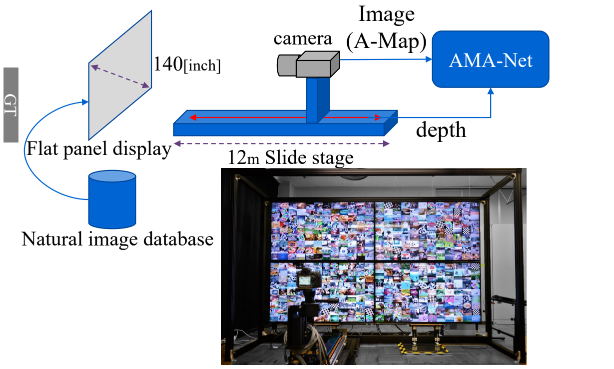

Figure 5. Experimental system. The 12m automatic slide stage is placed orthogonally to the display consisting of four 8K displays (total 140 inches, 15360 x 8640, 16K). RGB-DSLR camera is mounted on the stage moving with 1mm accuracy.

deep learning method is considered to effectively analyze complex A-Map.

3.3. AMA-Net

Archtecture. We developed A-Map analysis network (AMA-Net) to analyze aberration blur efficiently. AMA-Net architecture, shown in Figure 4, is based on ResNet [10], and it has two branches: gradient branch (main) and positional branch. Since A-Map contains various types of aberrations blur corresponding to position of image and distance information, we adopt patch-based architecture learning method [30, 26, 31, 21, 4, 3] to analyze only aberration blur. The architecture takes a patch extracted from a captured image as an input, and then outputs a single depth value corresponding to the patch. This network can be trained by patchwise images with flat depth data only. Such data can be collected easily by our experimental system (described in Section 4.1).

In the gradient branch as a main branch, the color gradient of an image patch is calculated with respect to the horizontal and vertical axis. All of the color gradients are concatenated to a position $x(i,j)$ in positional branch. It is well known that gradients give better results than color images do for blur analisys [5, 7, 23, 25, 24]. The network infers the defocus blur with learnable weight parameters θ as $\hat{b}(i,j) = f(x(i,j);\theta)$.

In the positional branch, the position (i,j) is broadcasted into the same size of the patch in order to handle the aberration position dependence.

We introduce the self-attention mechanism [32] which can put large weights on important features, therefore it allows to focus on aberration blur efficiently. In contrast to the main branch feature, this positional branch generates the attention maps. After concatenating the positional information to the gradients, the attention maps are calculated by sigmoid functions from each feature map.

The proposed networks are trained as a regression problem with supervision similar to stereo matching [13, 8] and DMDE [17, 2]. The ground truth distance $u(i,j)$ is converted to the blur radius $b(i,j)$ by using Equation 1. A tuple of $(k, x(i,j), u(i,j))$ is the element of a training dataset, where $k \in \{0, ..., K-1\}$ is the index. L1 loss function is defined as $L(\theta) = \frac{1}{N}\sum_k |b(i,j) - f(x(i,j);\theta)| (2)$, where N is the total number of training patches.

Implementation details. AMA-Net operates on an input patch size of 16x16 pixels with five Resblocks for each branch as shown in Figure 4. The convolutional layers in all of our networks have 3x3 kernels and 1 stride. The number of channels is fixed, 64 from the beginning to the end to avoid overfitting. The network parameters with the convolutional and fully connected layers are initialized randomly according to the approach of [18]. To train our networks, we use ADAM [15] with the default parameters $\alpha = 0.001, \beta_1 = 0.9, \beta_2 = 0.999, \epsilon = 10^{-8}$ and 128 as the batch size. Following [11], we do not use both L2 regularization on all model weights and dropout to the output of the last layer.

4. Experiment

First, we introduce settings of the experimental system for training and testing. Then we verify following items:

(1)Performance and robustness of our method (quantitative and qualitative evaluation).

(2)Validity of physical depth cue.

(3)Validity of AMA-Net's positional branch to handle position dependence of aberrations.

4.1. Settings

We developed an indoor experimental system for generating training and testing datasets, as shown in Figure 5. We put a disital single lens reflex (DSLR) camera (Nikon D810) with a f=50mm double-gauss lens (Nikon AI AF Nikkor 50mm f/1.8D) attached on the moving stage, then captured the images displayed on the screen. The captured image size is 7360x4912 pixel RAW. Meantime the distance from the camera was also recorded as ground truth. Before inputting images to AMA-Net, they were down-sampled to 1845x1232 to reduce learning costs. We fixed the focal distance at 1500mm and automatically captured 4 images at each 100 different distances (total 400 images) ranging from 1000mm to 2000mm. We carefully constructed our training recipe to analyze only blur information instead of contextual one. Therefore, we introduce various randomization techniques to our training recipe to make the deep network focus on blur information. We randomly picked images from the MSCOCO dataset [29] under various subject conditions, arranged in matrix form as shown in Figure 5. Horizontal or vertical flipping and random scaling was applied to each image to remove its shape and scale information. Several data augmentation techniques [16] are usually applied to avoid overfitting. For example, horizontal or vertical flipping, random scaling, and shearing are usually employed [6]. We select random crop [6], brightness [6] and random erasing [33] that do not affect blur. Note that this experimental system is not only for generating datasets but also for evaluation at a distance close to the outdoor scene.

4.2. Performance and Robustness results

Distance measurement. Regarding versatility, we evaluated our method by measuring the distance with lens aperture size (F value) of F1.8, F4 and F8 using the experimental system (Section 4.1). We used pre-trained model of each aperture and tested with images of MSCOCO dataset. Figure 6 shows estimated depth vs ground truth. The mean error at F1.8, F4 and F8 is 10, 20 and 46.3mm, respectively, which is roughly proportional to the F value. This is intuitively understandable because blur radius is basically inversely proportional to F value. From the results, we confirmed that our method can accurately estimate the depths.

Measurement range extension. Although we set the focus distance at 1500mm in the training, theoretically the blur radius is defined by relative distance from the focus distance, which means it can be normalized and applied to different measurement range. Thus, we shifted the focal distance from 1500mm to 6500mm for the longer measurement range. We obtained estimated depth without any modification, but simply multiplied it by 4.3. Figure 7 shows the error curves over the ground truth. The mean errors are also shown in the Figure 7. It also shows the depth accuracy with the basic stereo method as a reference.

The stereo method composed of two cameras with 250mm baseline. To get stereo depth, we used semi-global matching (SGM) [12] implemented in [1].

As the result shows, the mean error of F1.8 and F4 is equivalent to the stereo method F4. Therefore, our method can effectively apply to different measurement range without any additional training. The stereo camera has far stronger depth cue than our method (monocular) because of the large baseline. In contrast, the depth cue of our method is much smaller because the baseline is equivalent to 27.7mm in the stereo conversion. Despite the advantageous setting of the stereo, our method is comparably accurate except for the far plane. Although the mean error of F8 is 2.5 times larger than stereo method, still it has enough accuracy to tell the relative position between each object.

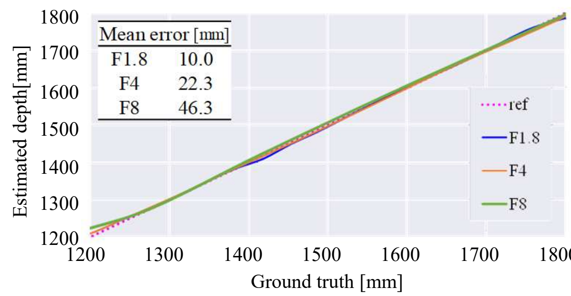

Figure 6. Estimated depth vs ground truth of apertures F1.8, F4 and F8. We set the focal distance to 1500mm (see Section 4.1).

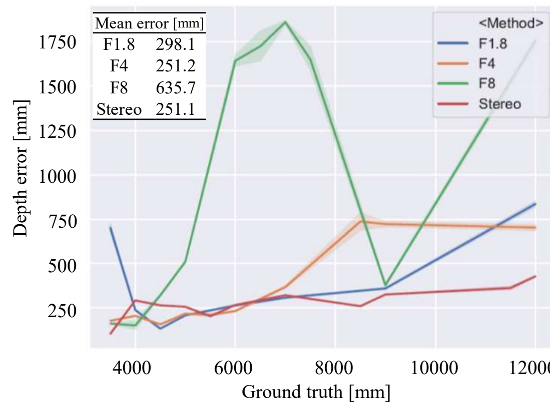

Figure 7. Comparison with our method and stereo method on the error curves vs ground truth. We set the focal distance to 6500mm.

Robustness in the wild. The robustness in another depth range test was carried out with focal distance 6500mm, and then depth accuracies were compared with contexture-based [20] and basic stereo method as a reference. We used the pre-trained AMA-Net that is trained with only the indoor dataset without any fine-tuning.

Figure 8 shows the qualitative results on outdoor scenes and human photos. From the results of context-based method, in the case of having contextual information such as sky or ground, it can estimate depth, as shown in Figure 8 (a) and (b). On the other hand, if there is no ground, as Figure 8 (c) and (d), large depth errors occurred. Moreover, when the whole human body is captured, errors often occur around the face area, as shown in Figure 8 (b) and (e).

As for the result with the stereo method, depth can be ac-

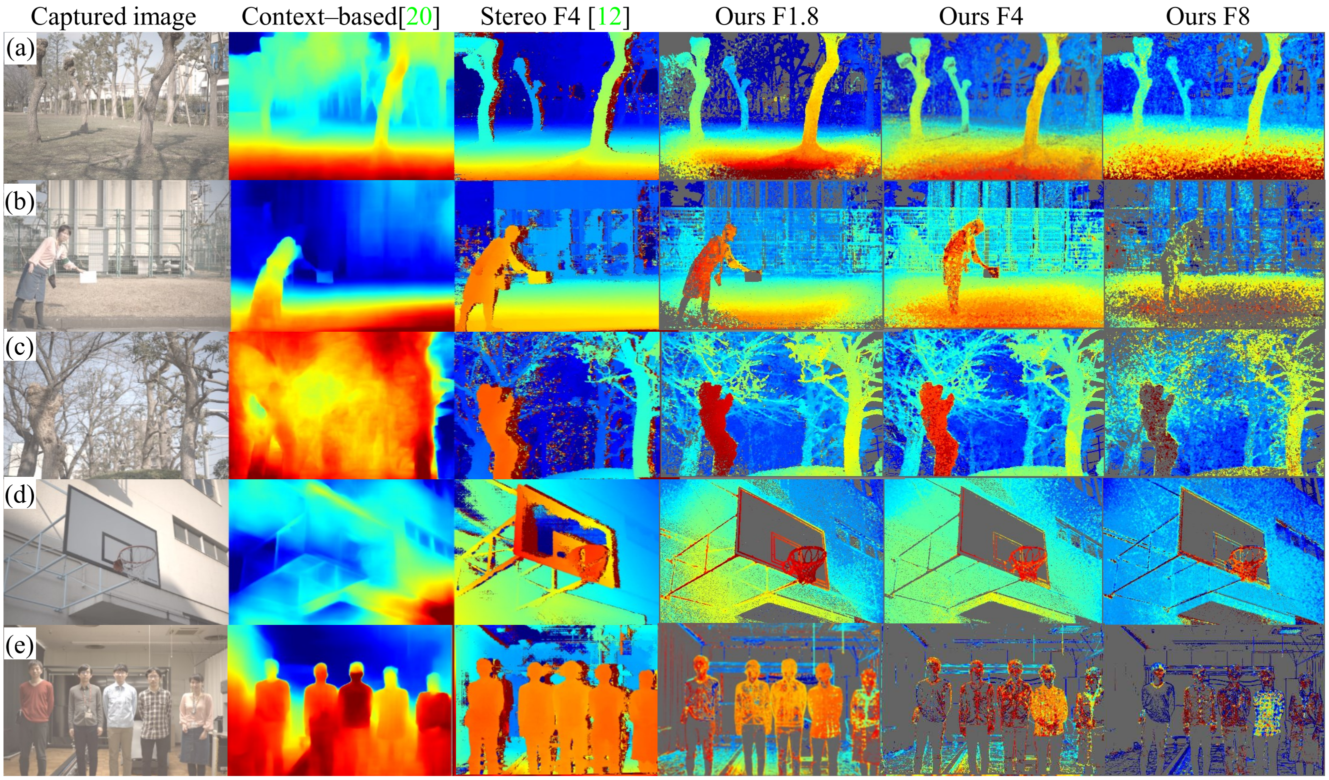

Figure 8. Qualitative results in the case of various outdoor scenes. We compare context-based, stereo method F4, and our method F1.8, F4 and F8. We used AMA-Net trained images only for indoor data taken by the experimental system without fine-tuning to the outdoor data. Gray indicates that there is no depth cue.

curately estimated, however, errors often occurred with occlusions, short distances, thin branches, or horizontal wire meshes.

In contrast, our method achieved accurate depth maps for the failure cases of both methods, especially, the wire mesh (Figure 8 (b)) and no ground image (c) and (d). Although the measurement range depends on training depth range, robust depth estimation was possible as we showed in Figure 7. Despite theoretical limitations, F8 still can estimate near and far depths. Some errors occur on the shading pattern such as clothes wrinkles (Figure 8 (e)), and lighting condition need to be adjusted, however, our method can estimate the depth of the whole human body's outline. In addition, a potential issue may arise by differences of spectral power distributions between display and natural scene irradiance. In places of direct sunlight, a purple fringe may be seen at wavelengths close to an ultraviolet range which TV light does not have. However, UV filters can be applied to cut such wavelength regions and solve the issue.

Scalability evaluation of other lenses. To evaluate the scalability to other lenses, we tested two different focal length lenses, f=24mm (AF-S NIKKOR 24mm f/1.4G ED) and f=105mm (AF-S VR Micro-Nikkor 105mm f/2.8G IF-ED). With these two lenses, we estimated the depth without any re-training, just applied the f=50m F4 pre-trained model as described in Section 4.1. Figure 9 (a) shows the depth map of trained f=50mm, (b) and (c) are the depth map applying the trained model of f=50mm to f=24mm and f=105mm respectively. We changed the focus distance individually to align the depth range.

The results of untrained lenses achieve reasonable depth, suggesting that geometric scaling is possible without retraining. Actually, most lenses share very similar characteristics on secondary ACA because this phenomenon arises from a refractive index dispersion of available glasses. Therefore, this relationship can be well maintained as the lens changes, then AMA-Net learns these characteristics. Thus, even a lens interchanges, it is possible to scale the depth by using such common properties. However, because aberrations depend on the lens specifications and the position in the lens, retraining each lens achieves more accurate depth.

4.3. Validity of physical depth cue

We verified the validity of physical depth cue based on the experimental system (Section 4.1). We used the following patterns for testing: (a) AR Maker pattern, (b) Step pattern, and (c) Color image. Each image has the correspond-

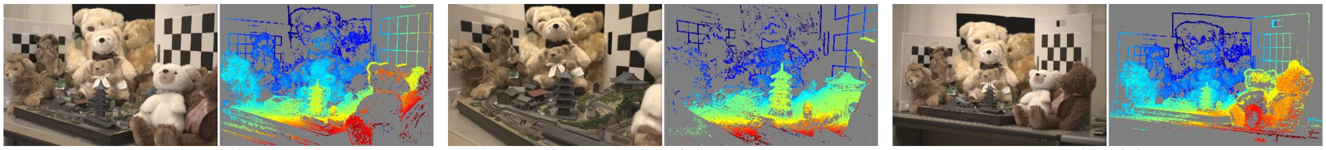

(a) Trained f=50mm (b) Untrained f=24mm (c) Untrained f=105mm

Figure 9. Scailability evaluation of three different focal length lenses: (a) Trained f=50mm, (b) Untrained f=24mm, and (c) Untrained f=105mm. All lenses were set to F4.

ing distance; thus, one image ideally has uniform depth. Figure 10 shows that our method correctly estimated depth of the near and far plane because the images show a uniform color for the corresponding plane, even there is no contextual information image as Figure 10 (b). Therefore, our method was not deceived by contextual information; we verified the validity of using aberrations as a depth cue.

4.4. Validity of AMA-Net's Positional branch

We tested the pre-trained model with and without a positional branch in AMA-Net (described in Section 3.3) in order to verify the validity of positional branch. We fixed the lens aperture F1.8. Figure 11 (a) presents an example of sampled A-Map. As can be observed from Figure 11 (a), the shape of PSF varies depending on the position. We chose the stripe pattern image, to simply analyze the position dependence of aberrations. The comparison of with and without a positional branch on depth estimation are shown in Figure 11 (b) and (c). The results demonstrated that the pre-trained model with the positional branch correctly (uniformly) estimated the depth, whereas many errors occurred on without the positional branch depth. The mean error of with positional branch is 10.0mm, that is about 2.5 times smaller than the error of without position branch (mean error: 25.1mm). As the result, we verified that the positional branch of AMA-Net can efficiently analyze all aberrations simultaneously.

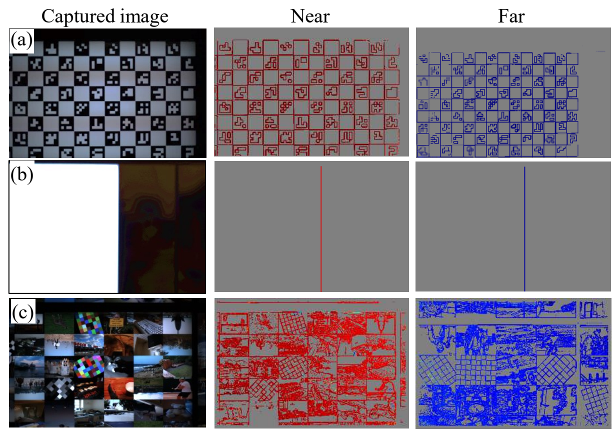

Figure 10. Estimated uniform depth of near and far plane.

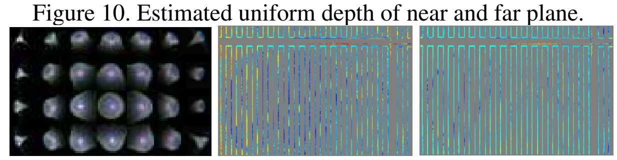

(a) Sampled A-map (b) OFF (c) ON

Figure 11. Comparison of estimated depth with and without the positional branch. (a) The sampled A-Map, (b) Without the positional branch, and (c) With the positional branch of AMA-Net.

5. Discussions

We have already presented the performance of our method above. From here, to discuss the validity of our method, we carried out simulation study, and then verified the following two items:

(1) Discrimination ability of various aberrations.

(2) Effectiveness of aberration type.

5.1. Simulation framework

We introduced a simulation framework, as shown in Figure 12. First, we convolved the PSF kernel obtained by the system (Figure 5) into the focus image to simulate the defocused image. We used the measured PSF because of the difficulty involved in simulating the lens (image) positional dependence on PSF. Variations of PSF to simulate defocused image are also shown in Figure 12 (A) - (E). The magnified images demonstrated the purple and green fringe on the edge of the near and far image which is equivalent to Figure 2 (E). Secondly, the simulated defocus image is passed to AMA-Net. As defocus images, we used MSCOCO dataset with a size of 1845x1232 pixels to match the experimental settings (Figure 5). Next, the simulated defocused images are input to AMA-Net for testing the pretrained model, and finally depth accuracy is estimated.

5.2. Discrimination ability of AMA-Net (sim)

To verify the AMA-Net's ability to discriminate various types of aberrations, first, defocused images were simulated using three types of PSF: (A) Mathematically defined pillbox shape, (B) Actual PSF at the image center, and (C) Actual PSF at the corner of the image (Figure 12). Next, we trained AMA-Net with (A) - (C) individually, then compared the estimated depth values under the following five conditions: (a) pre-trained A-model with A image, (b) pre-trained B-model with B image, (c) pre-trained C-model

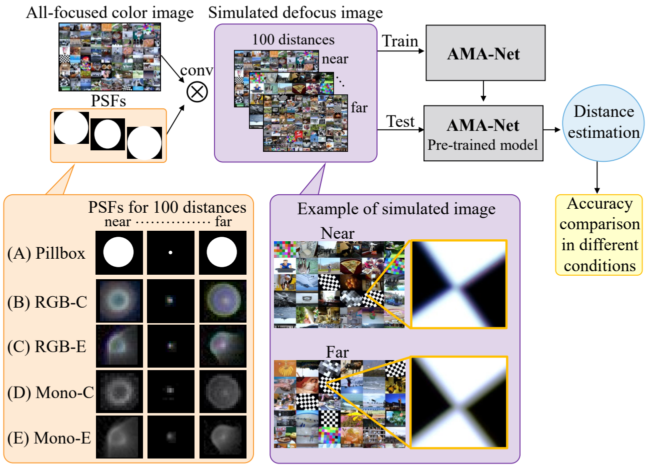

Figure 12. Simulation framework for depth estimation based on AMA-Net. We used five PSF variations: (A) pillbox and (B) - (E), the designations of which are RGB for full color PSF, Mono for Monochromatic PSF whose shape is the same as that of the Green PSF, C for Center of the image, and E for corner of the image.

with C image, (d) pre-trained B-model with C image, and (e) pre-trained C-model with B image. Only A is convoluted with a simulated PSF based on Equation 1, and the shape of which is pill box, imitating an ideal lens. B and C uses the center and corner PSF of the lens. In the case of (a) - (c) pre-trained models of PSF use for training and testing are identical, while (d) and (e) are cross-test to verify that AMA-Net is distinguishing different PSF shapes. Note that one type of PSF is convoluted in one entire image to individually verify aberration type only for simulation study.

Figure 13 shows the comparison of the estimated depth vs ground truth in the respective conditions (a) - (e). As for the results, (a) cannot accurately estimate distance because the ideal lens has no aberration synonymous with lack of depth cue. Moreover, (d) and (e) also have large errors in both the near and far planes, whereas (b) and (c) accurately estimate distance (equivalent to ideal line). However, (b) - (e) have slight difference near the in-focus plane because of the smallness of the PSF. From the results, AMA-Net can distinguish differences during analysis of the PSF.

5.3. Effectiveness of aberrations (sim)

To verified the effectiveness of aberrations, we compared the mean error of depth with various PSF shapes. Technically, aberrations have a position dependence on the lens (described in Section 3.2); therefore, we used following PSF kernels in training and testing images: (B) on-axis RGB-PSF, (C) on-axis Mono-PSF, (D) off-axis RGB-PSF, and (E) off-axis Mono-PSF, as shown in Figure 12 (B) - (E). RGB-PSF includes both a CA and MA feature, whereas, Mono-PSF has only MA. In this verification, we individually train our AMA-Net with images of (B) - (E) with F1.8

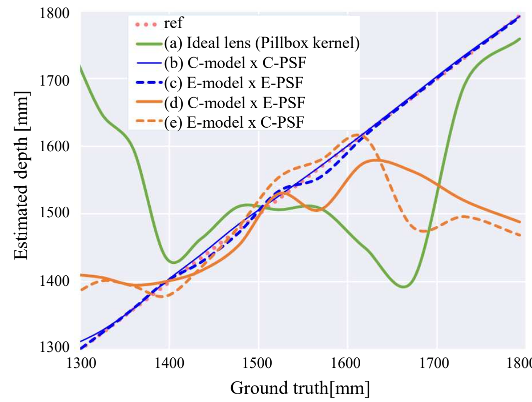

Figure 13. Comparison of estimated depth vs ground truth in five different conditions.

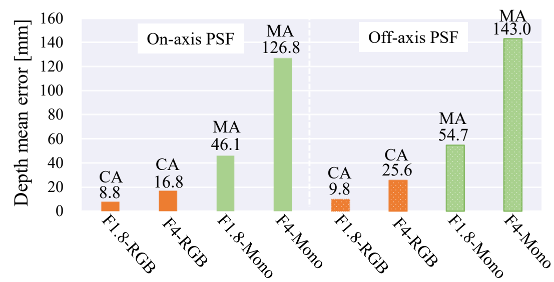

Figure 14. Comparison of estimated depth mean error on eight different types of PSF such as CA and MA in both on-axis and off-axis with F1.8 and F4, respectively.

and F4 PSF (see Figure 3). Figure 14 shows the comparison of the above four conditions of each F1.8 and F4 on the mean error of depth.

From the results, containing only MA still can be utilized as a depth cue; however, CA achieves even higher accuracy. Furthermore, on-axis and off-axis results denote the same tendency of depth mean error. That is to say, AMA-Net can analyze various types of aberration. Finally, we verified the effectiveness of CA and MA as a depth cue.

6. Conclusion

We have presented a novel method for passive single-shot depth measurement using only an off-the-shelf camera without customization or additional supportive devices. We have verified that A-Map, which contains various types of aberrations and distance information, can be utilized as a depth cue. We also have proposed AMA-Net that is additionally equipped with a self-attention-to-position mechanism to focus on only the aberration feature of A-Map. We demonstrated the effectiveness of A-Map for depth measurement through experimental and simulation analyses. The results of the experiments, supports this approach's achievement of highly accurate depth measurement and highly robust performance.

References

[1] OpenCV. https://opencv.org/. 5

[2] Amir Atapour-Abarghouei and Toby P. Breckon. Real-time monocular depth estimation using synthetic data with domain adaptation via image style transfer. In *The IEEE Conference on Computer Vision and Pattern Recognition (CVPR)*, June 2018. 1, 2, 4

[3] Christian Bailer, Tewodros Habtegebrial, Didier Stricker, et al. Fast feature extraction with cnns with pooling layers. *arXiv preprint arXiv:1805.03096*, 2018. 4

[4] Christian Bailer, Kiran Varanasi, and Didier Stricker. Cnn based patch matching for optical flow with thresholded hinge loss. *arXiv preprint arXiv:1607.08064*, 2016. 4

[5] Yosuke Bando, Bing-Yu Chen, and Tomoyuki Nishita. Extracting depth and matte using a color-filtered aperture. *ACM Transactions on Graphics (TOG)*, 27(5):134, 2008. 1, 2, 4

[6] Alexander Buslaev, Alex Parinov, Eugene Khvedchenya, Vladimir I Iglovikov, and Alexandr A Kalinin. Albumentations: fast and flexible image augmentations. *arXiv preprint arXiv:1809.06839*, 2018. 5

[7] Ayan Chakrabarti and Todd Zickler. Depth and deblurring from a spectrally-varying depth-of-field. In *European Conference on Computer Vision*, pages 648–661. Springer, 2012. 1, 2, 4

[8] Jia-Ren Chang and Yong-Sheng Chen. Pyramid stereo matching network. In *Proceedings of the IEEE Conference on Computer Vision and Pattern Recognition*, pages 5410–5418, 2018. 4

[9] Josep Garcia, Juan M. Sanchez, Xavier Orriols, and Xavier Binefa. Chromatic aberration and depth extraction. In *Proceedings 15th International Conference on Pattern Recognition. ICPR-2000*, volume 1, pages 762–765, 2000. 1

[10] Kaiming He, Xiangyu Zhang, Shaoqing Ren, and Jian Sun. Deep residual learning for image recognition. In *Proceedings of the IEEE conference on computer vision and pattern recognition*, pages 770–778, 2016. 4

[11] Alex Hernández-García and Peter König. Do deep nets really need weight decay and dropout? *arXiv preprint arXiv:1802.07042*, 2018. 4

[12] Heiko Hirschmuller. Accurate and efficient stereo processing by semi-global matching and mutual information. In *Computer Vision and Pattern Recognition, 2005. CVPR 2005. IEEE Computer Society Conference on*, volume 2, pages 807–814. IEEE, 2005. 5

[13] Alex Kendall, Hayk Martirosyan, Saumitro Dasgupta, Peter Henry, Ryan Kennedy, Abraham Bachrach, and Adam Bry. End-to-end learning of geometry and context for deep stereo regression. *CoRR, vol. abs/1703.04309*, 2017. 4

[14] Sangjin Kim, Eunsung Lee, Monson H Hayes, and Joonki Paik. Multifocusing and depth estimation using a color shift model-based computational camera. *IEEE Transactions on Image Processing*, 21(9):4152–4166, 2012. 1, 2

[15] Diederik P Kingma and Jimmy Ba. Adam: A method for stochastic optimization. *arXiv preprint arXiv:1412.6980*, 2014. 4

[16] Alex Krizhevsky, Ilya Sutskever, and Geoffrey E Hinton. Imagenet classification with deep convolutional neural networks. In *Advances in neural information processing systems*, pages 1097–1105, 2012. 5

[17] Yevhen Kuznietsov, Jörg Stückler, and Bastian Leibe. Semi-supervised deep learning for monocular depth map prediction. In *Proc. of the IEEE Conference on Computer Vision and Pattern Recognition*, pages 6647–6655, 2017. 1, 2, 4

[18] Yann A LeCun, Léon Bottou, Genevieve B Orr, and Klaus-Robert Müller. Efficient backprop. In *Neural networks: Tricks of the trade*, pages 9–48. Springer, 2012. 4

[19] Seungwon Lee, Nahyun Kim, Kyungwon Jung, Monson H Hayes, and Joonki Paik. Single image-based depth estimation using dual off-axis color filtered aperture camera. In *Acoustics, Speech and Signal Processing (ICASSP), 2013 IEEE International Conference on*, pages 2247–2251. IEEE, 2013. 1, 2

[20] Zhengqi Li and Noah Snavely. Megadepth: Learning single-view depth prediction from internet photos. In *Proceedings of the IEEE Conference on Computer Vision and Pattern Recognition*, pages 2041–2050, 2018. 5

[21] Wenjie Luo, Alexander G Schwing, and Raquel Urtasun. Efficient deep learning for stereo matching. In *Proceedings of the IEEE Conference on Computer Vision and Pattern Recognition*, pages 5695–5703, 2016. 4

[22] Carvalho Marcela, Saux Bertrand Le, Trouve-Peloux Pauline, Almansa Andres, and Champagnat Frederic. Deep depth from defocus: How can defocus blur improve 3d estimation using dense neural networks?? *european conference on computer vision*, pages 307–323, 2018. 1, 2

[23] Manuel Martinello, Andrew Wajs, Shuxue Quan, Hank Lee, Chien Lim, Taekun Woo, Wonho Lee, Sang-Sik Kim, and David Lee. Dual aperture photography: image and depth from a mobile camera. In *Computational Photography (ICCP), 2015 IEEE International Conference on*, pages 1–10. IEEE, 2015. 1, 2, 4

[24] Yusuke Moriuchi, Takayuki Sasaki, Nao Mishima, and Takeshi Mita. 23-4: Invited paper: Depth from asymmetric defocus using color-filtered aperture. In *SID Symposium Digest of Technical Papers*, volume 48, pages 325–328. Wiley Online Library, 2017. 1, 2, 4

[25] Vladimir Paramonov, Ivan Panchenko, Victor Bucha, Andrey Drogolyub, and Sergey Zagoruyko. Depth camera based on color-coded aperture. In *Proceedings of the IEEE Conference on Computer Vision and Pattern Recognition Workshops*, pages 1–9, 2016. 1, 2, 4

[26] Edgar Simo-Serra, Eduard Trulls, Luis Ferraz, Iasonas Kokkinos, Pascal Fua, and Francesc Moreno-Noguer. Discriminative learning of deep convolutional feature point descriptors. In *Proceedings of the IEEE International Conference on Computer Vision*, pages 118–126, 2015. 4

[27] Murali Subbarao and Gopal Surya. Depth from defocus: a spatial domain approach. *International Journal of Computer Vision*, 13(3):271–294, 1994. 2

[28] Pauline Trouve, Frederic Champagnat, Guy Le Besnerais, Jacques Sabater, Thierry Avignon, and Jereme Idier. Passive depth estimation using chromatic aberration and a depth

from defocus approach. *Applied optics*, 52(29):7152–7164, 2013. 1, 2

[29] Oriol Vinyals, Alexander Toshev, Samy Bengio, and Dumitru Erhan. Show and tell: Lessons learned from the 2015 mscoco image captioning challenge. *IEEE transactions on pattern analysis and machine intelligence*, 39(4):652–663, 2017. 5

[30] Sergey Zagoruyko and Nikos Komodakis. Learning to compare image patches via convolutional neural networks. In *Proceedings of the IEEE Conference on Computer Vision and Pattern Recognition*, pages 4353–4361, 2015. 4

[31] Jure Zbontar and Yann LeCun. Stereo matching by training a convolutional neural network to compare image patches. *Journal of Machine Learning Research*, 17(1-32):2, 2016. 4

[32] Han Zhang, Ian Goodfellow, Dimitris Metaxas, and Augustus Odena. Self-attention generative adversarial networks. *arXiv preprint arXiv:1805.08318*, 2018. 4

[33] Zhun Zhong, Liang Zheng, Guoliang Kang, Shaozi Li, and Yi Yang. Random erasing data augmentation. *arXiv preprint arXiv:1708.04896*, 2017. 5